Journal of Materials Chemistry A

Accepted Manuscript

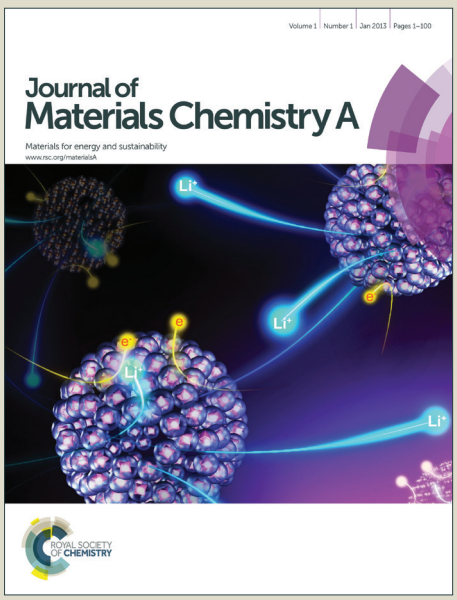

ROYAL SOCIETY OF CHEMISTRY

www.rsc.org/materialsA

Journal Name

RSCPublishing

ARTICLE

Low-temperature SnO_2-based electron selective contact for efficient and stable perovskite solar cells

Cite this: DOI: 10.1039/x0xx00000x

Received 00th January 2012,
Accepted 00th January 2012

DOI: 10.1039/x0xx00000x

www.rsc.org/

Jiaxing Song[a], Enqiang Zheng[b], Ji Bian[a], Xiao-Feng Wang[b]*, Wenjing Tian[a]*, Yoshitaka Sanehira[c] and Tsutomu Miyasaka[c]

We demonstrated compact SnO_2 thin films prepared by sinter-less spin-coating processes as an electron selective contact for $CH_3NH_3PbI_3$-based planar-heterojunction perovskite solar cells (PSCs). A modified sequential deposition method, in which the grain size of PbI_2 precursors was controlled by an equivalent solvent vapor annealing (SVA) process, was used to prepare the perovskite layer on SnO_2. With this SVA process, the remnant PbI_2 nanocrystals can stably occur at the interface of $CH_3NH_3PbI_3/SnO_2$ to carry out a passivation effect. The photovoltaic performance of SnO_2-based PSCs is dependent on both the SVA time and thickness of perovskite layer. The optimized PSC device achieves the best power conversion efficiency of up to 13% under the AM 1.5 simulated sunlight illumination, which is highly durable over 30 days of storage time with exposure to the ambient air environment.

1. Introduction

Amongst the next-generation photovoltaic technologies being developed nowadays, $CH_3NH_3PbX_3$ (X = Cl, Br, I)-based perovskite solar cells (PSCs)are the most shining star because of their rapidly boosted power conversion efficiency (PCE), their cost-effectiveness, and their scalable processability.[1-6] The investigations focused on the perovskite materials have revealed their superior opto-electrical properties including suitable band-gap, high absorption coefficient, and extremely long and balanced ambipolar carrier transport.[7-11] In spite of the large potential of perovskite materials, the photovoltaic performance of PSCs was always sensitive to many factors, e.g., the device configurations, the producing method of perovskite layer, the materials employed as the charge extraction contacts, and even the moisture level during the PSCs preparation.[12-20] Before a consensus in PSC devices could be reached, explorations toward all the aspects of PSCs will help in the knowledge accumulation.

The exploration ofthe materials used as the electron selective contact (ESC) for PSCs remains one of the most challenging scientific issues. Although many inorganic semiconductors may be feasible as ESCs materials for PSCs, to the best of our knowledge, a majority of researches into PSCs so far focuses mainly on TiO_2 and ZnO.[21-28] The opto-electrical properties between these two semiconductors are too similar to differentiate the electron transport mechanisms at the perovskite/ESC interface.

Compared to those TiO_2 and ZnO, Tin oxide (SnO_2) is similar with the wide band-gap, high transparency, and large electron mobility, but exhibit lower energy for the conduction-band edge (CBE).[29-32] The fact that the SnO_2 thin films could give sufficient conductivity without higher temperature sintering process will benefit a future fabrication of the photovoltaic device on plastic substrates. Importantly, it was found in the previous investigation that SnO_2 is much effective in collecting electrons with low energy than TiO_2 resulting in substantially improved photocurrent in electrochemical cells.[33] Similarly, some low-energy charge carriers of narrow band-gap perovskite absorbers consisting tin metal or formamidium in their structure may not efficiently be collected by TiO_2 or ZnO, but be collected by SnO_2. Thus, the study of SnO_2 as ESC for PSCs will provide an important piece of information in further development of this photovoltaic device to efficiently utilize long wavelength photons.

A general concern with the use of SnO_2 as ESC, however, is that the voltage of PSCs may be decreased accordingly as the low CBE of SnO_2 may reduce a built-in potential of Schottky barrier between the perovskite and ESC layers. This problem could be solved through surface passivation, as suggested by many previous investigations on TiO_2-based PSCs.[34-35] It was found that the presence of PbI_2 species in the grain boundaries upon thermal annealing can lead to a successful passivation of

$CH_3NH_3PbI_3$ films, resulting in improved carrier electric property and thus device performance.[35-36] The mechanism of this passivation effect by PbI_2 was further revealed by the femtosecond time-resolved transient absorption spectroscopy.[37] Nevertheless, the fact that PbI_2 passivation was achieved by decomposition of $CH_3NH_3PbI_3$ in these investigations may be accompanied by improvement of PSC's durability.

In this investigation, we employed SnO_2 thin films prepared by spin-coating of nanoparticles as ESCs to fabricate low-temperature-processed PSCs. We modified the typical two-step deposition technique by introducing slow growth of the PbI_2 precursor with solvent vapors to control the crystal growth of perovskite. Intriguingly, we observed the variation in absorbance and grain size of PbI_2 with different solvent vapor annealing times. The varied PbI_2 precursor results in a clear variation in the surface morphology, grain size, and absorbance of corresponding perovskite layer. Importantly, the constantly occurred PbI_2 layer on the interface of perovskite/SnO_2 shows no negative effect to the photovoltaic performance of the resulting PSCs. Optimization of the$CH_3NH_3PbI_3$ film thickness has delivered a maximum PCE of 13.0% under the standard air mass AM 1.5G light illumination. Most importantly, the SnO_2-based PSCs exhibited high stability against ambient air without encapsulation. This study will contribute to both a deeper understanding of the mechanism and the real-world applications of the PSC technology.

2. Experimental

2.1 Materials

The SnO_2 nanoparticles (ca. 22 ~ 43 nm) were purchased from Wako Chemicals. The lead iodide (beads, -10 mesh, 99.999% trace metals basis) and lithium salts (>99.0%) were purchased from Aldrich. The CH_3NH_3I (>99.0%) was purchased from Xi'an Polymer Light Technology Corp. (PLT). The Spiro-OMeTAD (2,2',7,7'-tetrakis-(N,N-di-4-methoxyphenylamino)-9,9'-spirobifluorene, >99.0%) was purchased from Merck. Ultradry solvent of N, N-dimethyl formamide (DMF, >99.9%) and isopropanol (> 99.9%) were obtained from *J&K* and Acros, respectively. All the chemicals and solvents keep in the glove-box before starting our experiment.

2.2 Device fabrication

The pre-patterned ITO substrates were cleaned with detergent, deionized water, acetone, and 2-propanol in sequence. The SnO_2 nanoparticles were dispersed in butanol with a concentration of 6 mg/ml and stirred for 3 hours before use. The solution was filtered with a PVDF hydrophobic 0.45um filter and spin-coated on ITO substrates at 3000 rpm for 30s to form a relatively compact SnO_2 thin layer, and followed by short baking at 150℃ for 5 min. This procedure was repeated for three times before finally baking at 200℃ for 1 hour. A 460 mg/mL solution of PbI_2 in DMF was then spin-coated on the top of the SnO_2 layer at 3000 rpm for 30s in the glovebox. The PbI_2-coated SnO_2 thin films was kept in a petri dish for x minutes (x = 1, 10, 20, 35, and 50) allowing a slow growth of PbI_2 nanoparticles, and was followed by annealing at 70℃ for 30 min. After cooling to room temperature, the films was dipped into a CH_3NH_3I 2-propanol solution (10 mg/mL) for 50 s, and was followed by annealing at 70℃ for 20 min to give a desired crystallite formation. As the hole-transporting material (HTM), 80 mg/mL solution of Spiro-OMeTAD in chlorobenzene was spin-coated at 4000 rpm on the $CH_3NH_3PbI_3$ containing 46.5μL Li-TFSI and 10.5 μL tert-butylpyridine per milliliter. The substrates with HTM were left overnight in the dry air in dark at room temperature. Finally, 100 nm thick Ag was thermally evaporated on the top of HTM to produce a completed PSC device.

2.3 Device characterization

The current–voltage characteristics of solar cells were measured by a computer-controlled Keithley 2400 source meter measurement system with an AM1.5G filter at a calibrated intensity 100mWcm^{-2} illumination, as determined by a standard silicon reference cell (91150V Oriel Instruments). The effective area of the cell was defined to be 0.04 cm^2 using a non-reflective metal mask. IPCE spectra was measured in airunder short-circuit conditions using a commercial IPCE setup (Crowntech QTest Station 1000AD), which was equipped with a 100W Xe arc lamp, filter wheel, and monochromator. Monochromatedlight was chopped at a frequency of 80 Hz and photocurrents measured using a lock-in amplifier. The setup was calibrated against a certified silicon reference diode.

2.4 Thin film characterization

Film thicknesses were measured using a Veeco Dektak 150 surface profilometer. UV-Vis-NIR spectra were measured on a Shimadzu UV-2550 spectrophotometer. The X-ray diffraction (XRD) patterns were recorded on Rigaku SmartLab X-ray diffractometer with Cu Kα radiation (λ = 1.5418 Å) at 25℃. The data were collected with a 0.01°step size (2θ). A field emission scanning electron microscope (Hitachi SU8020) was used to acquire SEM images.

3. Results and discussion

3.1 Sequential deposition of $CH_3NH_3PbI_3$ on SnO_2 ESCs

Fig. 1a shows the X-ray diffraction (XRD) pattern of the SnO_2 nanoparticles used in this investigation. Each of these diffraction lines are commonly assigned to the tetragonal rutile crystalline phases of SnO_2.[38] Fig. 1b shows the high magnification scanning electron microscope (SEM) image of the SnO_2 thin films prepared by spin-coating of the SnO_2 nanoparticles. The SnO_2 film is very thin and does not have typical porous structure so that the following study of PSCs is likely based on a planar-heterojunction configuration. Both the lower and higher magnification SEM images of SnO_2 film are also shown in Fig. S1.

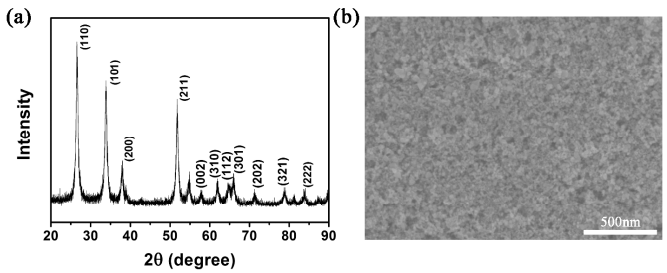

Figure 1. (a) The XRD pattern of the SnO_2 nanoparticles, and (b) the high magnification SEM image of SnO_2 film on ITO.

A two-step sequential deposition method was employed to produce the $CH_3NH_3PbI_3$ perovskite layer on this SnO_2 film, as schematically shown in Fig. 2. To maintain PbI_2 layer with good crystallinity for effective passivation of the $SnO_2/CH_3NH_3PbI_3$ interface, a modified method to prepare the PbI_2 films was introduced as detailed in the Experimental section.[34] As shown in Fig. 3a, with different aging time of wet PbI_2 films in N_2 atmosphere in covered petri dish, the appearance of PbI_2 films gradually changes from transparentred-yellow with 1 min to opaque dark-yellow with 50 min. This process could be regarded as an equivalent process of solvent vapor annealing (SVA) as suggested by previous investigation on organic solar cells.[39] In order to clarify the difference in the film appearances, the XRD patterns of the PbI_2 films were measured and are shown in Fig. 4. With elongated SVA time, the density of the most representive XRD peak of the PbI_2 nanocrystals at $2\theta = 12.56°$ gradually increases together with the narrowing of the full-width-at-half-maximum (FWHM). The enlarged XRD peak of the PbI_2 nanocrystals at $2\theta = 12.56°$ is shown in Fig. S2. We employed Scherrer formula, i.e., $D=K\lambda/(\beta\cos\theta)$, to calculate the grain size of the PbI_2 nanocrystals. Here, the Scherrer constant, K, is 0.943, and the X-ray wavelength, λ, is 0.15406 nm. The FWHM of this diffraction peaks in digits is 0.39671, 0.25951, 0.22059, 0.20612, and 0.19980, which corresponds to the PbI_2 crystalline size of 21.1, 32.3, 38.0, 40.6, and 41.9 nm for SVA times of 1, 10, 20, 35, and 50 min, respectively. The PbI_2 crystallite size increases with increased SVA time of the PbI_2 films, and the growth of the crystallite size is especially severe in the first 20 min. The SEM images of PbI_2 film surfaces with different SVA time are also depicted in Fig. 5, and in Fig. S3 of the supporting information with low magnification. Generally speaking, it is difficult to identify the crystallite size of each PbI_2 crystal from the SEM image, because these PbI_2 nanocrystallite aggregate along the surface forming large domains. Interestingly, the domain size of PbI_2 multi-crystals gradually increases with increased the SVA time. Noticeably, there is no distinguishable cavities for the PbI_2 film with 1 min SVA time, whereas numbers and sizes of the cavity on the surface of the PbI_2 film increases with further increasing SVA time until 50 min. It is expected that PbI_2 films with more cavities must be more capable for the CH_3NH_3I solution penetration during the dipping process of the sequential method. Therefore, PbI_2 films with longer SVA times will be more reactive with CH_3NH_3I to produce perovskite layer than those with shorter SVA times during a certain period of time.

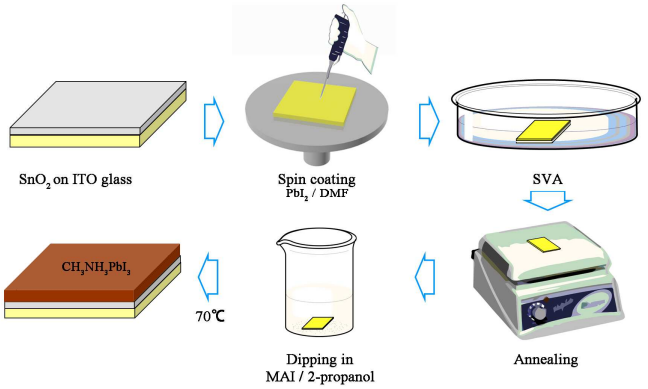

Figure 2. Schematic illustration of the modified two-step sequential deposition method for preparing perovskite films.

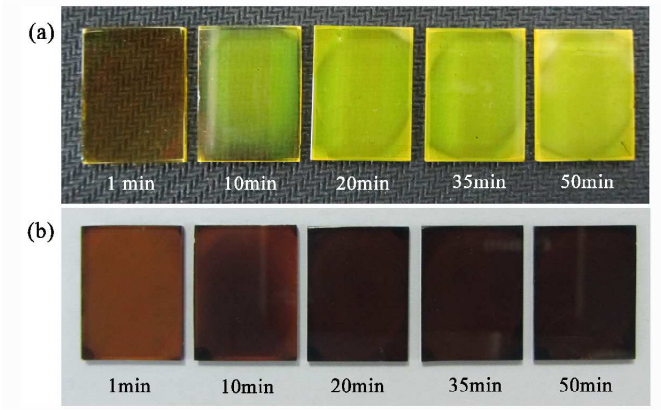

Figure 3. Photographs of ITO/SnO_2/PbI_2 films (a), and corresponding ITO/SnO_2/$CH_3NH_3PbI_3$ films (b) with different SVA times for PbI_2 layers.

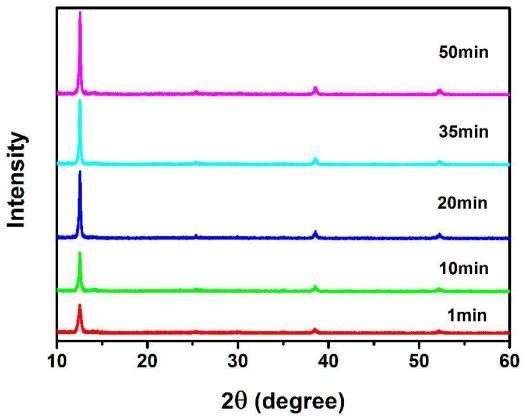

Figure 4. X-ray diffraction patterns of ITO/SnO_2/PbI_2 films with different SVA time for PbI_2 layers.

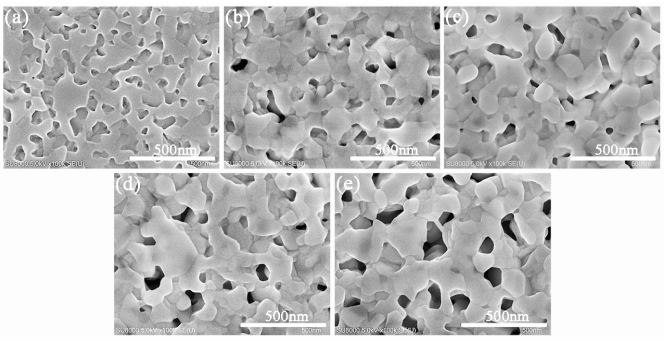

Figure 5. SEM micrographs of ITO/SnO_2/PbI_2 thin films for different SVA times (a) 1min, (b) 10 min, (c) 20 min, (d) 35 min, and (e) 50 min.

The variation of crystallite size and compactibility of the PbI_2 films must influence on the perovskite film formation. Fig. 2b shows the photo images of perovskite films prepared by dipping these SVA treated PbI_2 films into CH_3NH_3I solution for 50 s. The perovskite films gradually changes from light-brown to dark-black in color with increased SVA time. Fig. 4 shows the electronic absorption spectra of the corresponding $CH_3NH_3PbI_3$ films. The absorption of the perovskite films increases throughout the long wavelength region with increased SVA time, except for that of the perovskite film obtained from 1 min SVA time, in which the absorption of PbI_2 is still predominant. The absorption spectra of these perovskite films are consistent with their photo images indicating that more PbI_2 is converted into $CH_3NH_3PbI_3$ with increased SVA time. The absorption spectra is consistent with the observation of the increased porosity in the PbI_2 films with increased SVA time, because CH_3NH_3I is more conductive to infiltrate into the inner of PbI_2 layer in the case of PbI_2 films with more cavities.

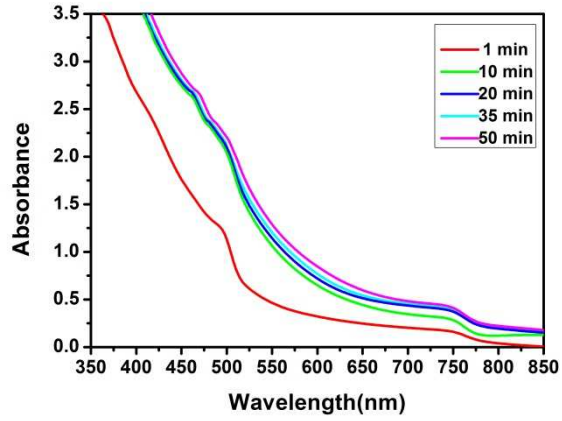

Figure 6. UV-vis-NIR absorption spectra of $CH_3NH_3PbI_3$ thin films obtained from the PbI_2 layers with different SVA time.

The significant difference in the absorption spectra of perovskite films might be an implication of different film morphology. The SEM images of the perovskite films obtained from PbI_2 layers with different SVA time are depicted in Fig. 7. The average grain diameter of the perovskite crystals increases as the SVA time of PbI_2 films increases; The change in the morphology is particularly significant between the SVA times of 1min and 10min. Obviously, the grain size of perovskite crystals is dependent on that of the PbI_2 crystals, i.e., the smallest 21.1 nm PbI_2 crystal obtained from 1 min SVA time produces the smallest $CH_3NH_3PbI_3$ crystal, whereas the largest 41.9 nm PbI_2 crystal obtained from 50 min SVA time produces the largest $CH_3NH_3PbI_3$ crystal. It is naturally expected, therefore, that the formation of $CH_3NH_3PbI_3$ crystal must be accompanied by the consumption of PbI_2 crystals. This process is usually seeable from the XRD patterns of the perovskite films as studied by many previously investigations.[21,25,34] The XRD pattern of the perovskite films were also measured and shown in Fig. 8. In the XRD patterns, the newly generated 2θ peaks appearing at each 14.0°, 24.3°, 28.4°, 31.7° and 50.3° correspond to the (110), (202), (220), (310) and (404) planes of the tetragonal phase of $CH_3NH_3PbI_3$, respectively.[40] Interestingly, the XRD peak of the PbI_2 nanocrystals at 12.56° has negligible changes after the generation of the $CH_3NH_3PbI_3$ crystals. Given that there have been definitive evidences (absorption spectra and SEM images) directing to a large yield of perovskite from raw PbI_2 during the dipping process, the only interpretation to the strong PbI_2 signals in the XRD pattern of the perovskite films is that the remaining PbI_2 in the perovskite films has kept with high crystallinity; From this point of view, the 001 plane (12.56°) of the PbI_2 crystal must be less reactive with CH_3NH_3I. The remaining PbI_2 crystals are likely occurring at the interface of $CH_3NH_3PbI_3$ and SnO_2 ESC, because the reaction of PbI_2 film with CH_3NH_3I in solution is a diffusion limited process. Compared to previously reports that their PbI_2 phase were presented in all perovskite grain boundaries and at the relevant interfaces,[36-37] the occurrence of PbI_2 crystals in our perovskite layers is more specifically acting as a passivation layer for charge transportation/recombination at the perovskite/SnO_2 interface.

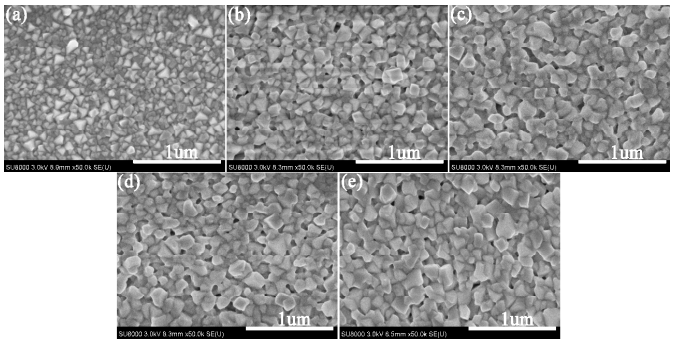

Figure 7. SEM micrographs of ITO/SnO_2/$CH_3NH_3PbI_3$ thin films obtained from PbI_2 layers with different SVA times (a) 1min, (b) 10 min, (c) 20 min, (d) 35 min, and (e) 50 min.

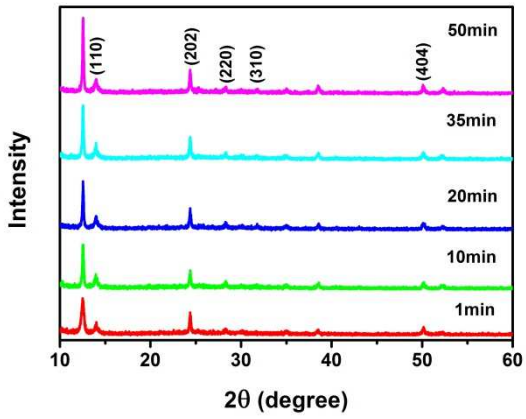

Figure 8. X-ray diffraction patterns of ITO/SnO_2/$CH_3NH_3PbI_3$ thin films obtained from the PbI_2 layers with different SVA time.

3.2 Photovoltaic performance and durability of SnO_2-based perovskite solar cells

Although above detailed characterization of the perovskite layer on SnO_2 has concluded that high crystalline PbI_2 remains constantly at the interface throughout different SVA times, this rare situation is not ever seen in any high efficiency PSCs reported so far. In fact, some investigations suggested the presence of PbI_2 would lead to poor photovoltaic performance.[41-42] To know whether this design is feasible for the device performance, PSCs were fabricated with SnO_2/perovskites examined in the previous section. For the convenience of comparison, the perovskite layer was fixed at 190 nm for all PSCs. Fig. 9a shows the PSC device configuration based on the SnO_2 ESC. As the hole-transporter, the typical Spiro-OMeTAD was employed. Fig. 9b shows the energy alignment of each component in the PSC devices.[32,34,43] Here, the energy level of PbI_2 is nicely aligned between that of both SnO_2 and $CH_3NH_3PbI_3$ indicating that PbI_2 may be not only retarding the reversed electron leakage but also mediating the electron transportation from perovskite to SnO_2. Fig. 10 shows a typical cross-sectional SEM image of perovskite solar cell device obtained from PbI_2 film with 10 min SVA time. Although the presence of pure PbI_2 crystals in the perovskite layer is proven by the XRD patterns, the occurrence of either the pure PbI_2 or the boundary of perovskite/SnO_2 interface is quite misty.

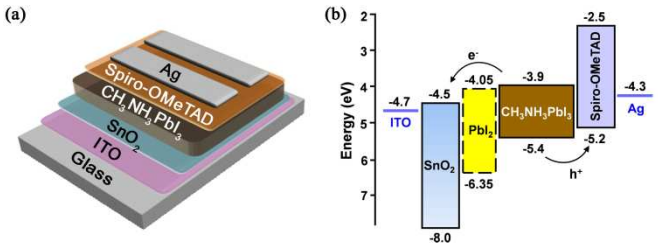

Figure 9. Device architecture (a) and energy diagram (b) of the ITO/SnO_2/$CH_3NH_3PbI_3$/spiro-OMeTAD/Ag cells tested in this study.

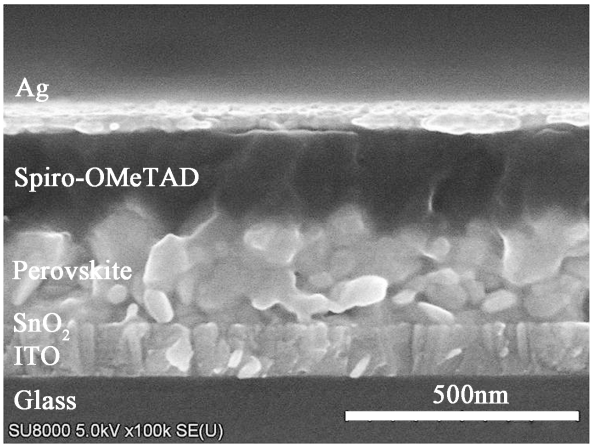

Figure 10. Cross-sectional SEM image of a PSC device based on SnO_2 ESC.

Fig. 11a shows the current-voltage (*J–V*) characteristics (sweeping from the open-circuit to the forward bias) of PSCs with different perovskite layers. Table 1 lists the parameters directly obtained from the *J-V* curves. As can be seen from the data, all the performance-related parameters including the short-circuit current (*J*sc), the open-circuit voltage (*Voc*), the fill factor (FF), and PCE are all poor for the device corresponding to the PbI_2 with 1 min SVA time. As the SVA time increases, the *J*sc, *V*oc, and FF reached their maximum value at 20, 10, and 10 min, respectively. The gradually decreased *Voc* and FF with increased SVA time of PbI_2 films from 10 min to 50 min may be due to the decrease of the amount of remnant PbI_2 in perovskite films. We suppose that remnant PbI_2 suppresses detrimental electron-transfer processes to cause charge recombination/interception, and acts as a passivation effect for surface defects and charge carrier trapping so as to enhance *Voc* and shunt resistance, as also suggested by previous investigation.[36] Moreover, the perovskite film quality seems the highest with 10 min SVA time suggesting the film quality may plays role in determining the photovoltaic performance. The highest PCE of 12.3%, determined with a *J*sc =18.8 mA cm^{-2}, a *V*oc = 1.08 V, and a FF =0.60, was achieved for perovskite layer obtained from 10 min SVA time of PbI_2. Fig. 11b shows the incident photon-to-current efficiency (IPCE) spectra of the corresponding devices in Fig. 8a. The photocurrent as integrated area under the IPCE spectra is in good agreement with the *Jsc* values obtained from the *J-V* characteristics. For the PSC based on PbI_2 with 1 min SVA time, the IPCE values are low over the whole spectrum. In particular, the IPCE response signal was not from the absorption of $CH_3NH_3PbI_3$ but from that of PbI_2. In this case, PbI_2 layer must function as an insulation layer for the perovskite free-carriers, whereas it seems that some free-carriers generated in the PbI_2 layer can somehow be extracted by the electrodes. For the other PSCs with longer SVA times in PbI_2 preparation, the charge carriers of perovskite layer were efficiently extracted by the electrodes, indicating the PbI_2

crystallite at the interface of $CH_3NH_3PbI_3/SnO_2$ does not disturb the electron extraction by SnO_2. Besides, the IPCE values of the optimal device reach more than 70% across a broad range of wavelength proving excellent light-harvesting and quantum conversion by the device. In order to evaluate the composition of PbI_2 in perovskite layer in the best performing solar cells, the EDX (Energy Dispersive X-Ray Spectroscopy) analysis was also carried out for the perovskite layer obtained from the PbI_2 with 10 min SVA time (the EDX patterns are shown in Fig. S4). The resultant atom% of the Pb and I element is 25.7 and 74.3, respectively, and the atom ratio of Pb and I is approximately 1:2.9. We thus roughly calculated the fraction of PbI_2 is ~10% in the perovskite layer, which indicates the $CH_3NH_3PbI_3$ is still predominantly more than the remnant PbI_2.

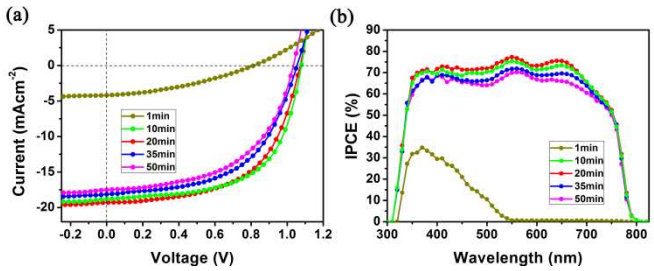

Figure 11. *J–V* curves (a) and IPCE spectra (b) of the ITO/SnO_2/$CH_3NH_3PbI_3$/spiro-OMeTAD/Ag devices based on the PbI_2 layers with different SVA time.

Table 1. The corresponding photovoltaic performance parameters for PSCs in Figure 8a.

SVA Time(min)	*Voc*(V)	*Jsc*(mAcm^{-2})	FF(%)	PCE (%)
1	0.81	4.0	36.6	1.2
10	1.08	18.8	60.3	12.3
20	1.07	19.3	57.6	11.9
35	1.05	18.1	55.1	10.8
50	1.03	17.5	54.0	9.7

Given that with the same SVA time for PbI_2, the $CH_3NH_3PbI_3$ thickness is a constant value after a certain dipping time for PbI_2 in CH_3NH_3I solution, the amount of PbI_2 left on the $CH_3NH_3PbI_3/SnO_2$ interface will depend on the amount of initial PbI_2 reactant. We thus prepared the initial PbI_2 layer with different thickness, and followed by a 10 min SVA time to fabricate PSCs. In Fig. 9, we plotted the *Voc*, *Jsc*, FF and PCE values as a function of total perovskite film thickness. Generally speaking, the *J*sc value increases with increased perovskite thickness, whereas in our experiments optimal *V*oc and FF values were found at the perovskite thickness of ca.190 nm. The averaged PCE reaches the maximum level at ca.240 nm thick perovskite layer with a value of 12.0±0.6%. These results indicate that adjusting the thickness of the crystallite PbI_2 layer will balance a series of processes including free carrier generation and carrier transportation/extraction.

As shown in Fig. 13, a champion PCE of 13.0% was achieved with a *Voc* of 1.08 V, a *Jsc* of 19.5 mA cm^{-2}, and a FF of 0.62, upon the optimization of the SVA time and the thickness of PbI_2. This result is comparable with PSCs studied for TiO_2 and ZnO having a planar-heterojunction configuration. Given that SnO_2 has a much deeper CBE than those TiO_2 and ZnO ESCs, this study provides a unique model system for studying those PSCs with narrow band-gap perovskite materials.

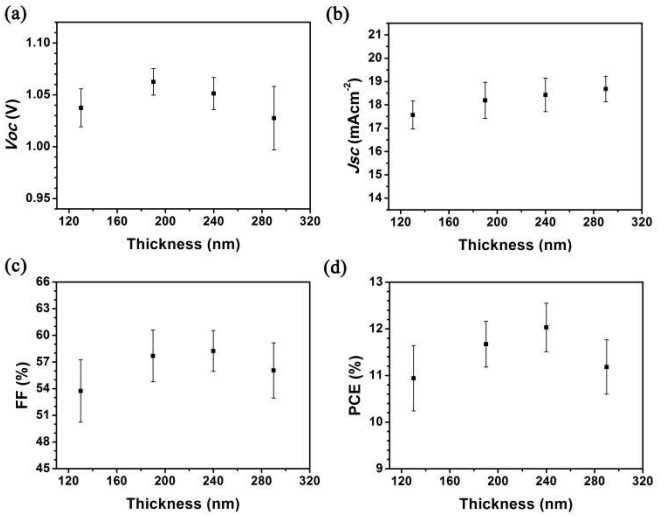

Figure 12. (a) *Voc*, (b) *Jsc*, (c) FF and (d) PCE as a function of perovskite film thickness (ca.130, 190, 240 and 290nm). Data are derived from measurements on 10 separate devices.

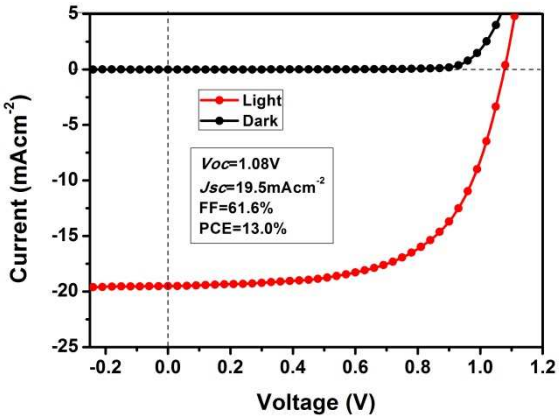

Figure 13. (a) *J-V* characteristic for the highest-performing ITO/SnO_2/$CH_3NH_3PbI_3$/spiro-OMeTAD/Ag device measured under 100 mWcm^{-2} AM 1.5G illumination and in the dark.

It was reported by some research groups that PSCs based on the planar-heterojunction architectures are unstable over time even without constant light soaking.[19,43] It was a mystery that devices based on either TiO_2 or ZnO degraded significantly to 10%-30% of the initial value after only dozens of hours storage, no matter what atmosphere the devices are stored in.[19,43] We also wonder if the planar-heterojunction PSCs studied in the present research are stable in the ambient air. Fig.14 shows stability result of the SnO_2-based device stored in ambient air environment. The PCE of the SnO_2-based PSC keeps almost constant over 700 hours; In comparison, a PSC device based on compact TiO_2[12] (see Fig. S5 in the supporting information for its photovoltaic performance) with planar-heterojunction

prepared with same sequential deposition method degrades apparently faster than the SnO_2-based devices. This excellent durability of SnO_2-based PSC may be partially originated from the remnant PbI_2 that prevent direct contact of SnO_2 and $CH_3NH_3PbI_3$ to reduce the possible degradation of $CH_3NH_3PbI_3$ through charge injection (as the TiO_2-based PSC also shows improved durability compared to the reference results[19]). We speculate that the lower hygroscopicity of the SnO_2 compared with TiO_2 also contributes to the durability of the PSC device. In addition, both oxygen vacancies and UV light induced degradation in TiO_2 are well-known problems to reduce the stability of TiO_2-based photovoltaic devices.[44] In the present investigation, the hole selective contact is the commonly used material, i,e., spiro-OMeTAD. Thus, the durability of devices will be severely affected by the spiro-OMeTAD layer. In fact, our PSC devices, no matter with what kind of electron selective contact, degrade significantly after 1-2 months after the preparation being mainly attributable to the degradation of spiro-OMeTAD. Fortunately, some inorganic hole selective contact materials, such as CuSCN and CuI,[45-47] gives improved stability than the spiro-OMeTAD, indicating our SnO_2-based PSCs have larger potential in the real-world applications.

Finally, one of the reviewers suggested to preliminary examine the photo-stability of the SnO_2-based PSCs. Fig. S6 in the supporting information shows the durability result of the device under simulated sunlight illumination. The PCEs of PSC devices based on both SnO_2 and TiO_2 decrease significant under the simulated sunlight illumination within merely 8h, in spite that the SnO_2-based device is slightly more stable than the TiO_2-based device. Interestingly, the photovoltaic performance of these PSC devices is recoverable after a storage of the devices in dark for 18 hours, indicating that the reduction of photovoltaic performance upon light illumination of the PSC devices is not due to the degradation of materials, but may be due to the ferroelectric nature of perovskite materials that accumulate charge carriers at the interface to interfere the electricity flow at the working condition.

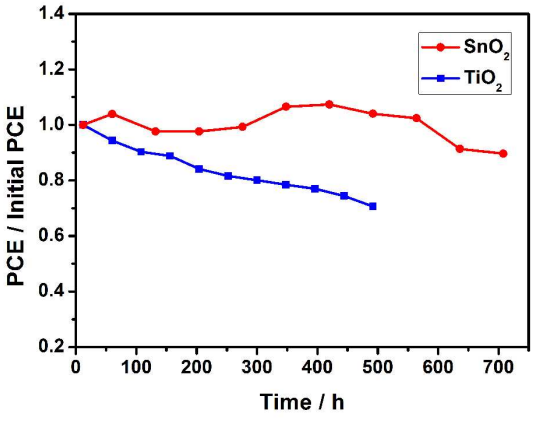

Figure 14. Durability of the SnO_2-based and TiO_2-based PSC device exposed to ambient air. The test was on the devices without encapsulation.

Conclusions

In summary, we have developed SnO_2 thin films as electron selective contacts for $CH_3NH_3PbI_3$-based perovskite solar cells. During the process of perovskite preparation, we observed the variation of grain size of PbI_2 layer that is dependent on the solvent vapor annealing time resulting in morphological and absorbance changes in the corresponding perovskite films. The remnant PbI_2 crystallites at the $SnO_2/CH_3NH_3PbI_3$ interface carry out a passivation effect, which is supposed to improve the photovoltaic performance of perovskite solar cells. By optimization of the solvent vapor annealing time and the thickness of perovskite layer, the SnO_2-based devices achieved a highest power conversion efficiency of 13.0%, which is highly durable with exposure to the ambient air environment for 30 days. This combination of ease-of-fabrication, low-temperature processing, efficient performance and excellent durability are all expected to help promote the development of the novel photovoltaic technology for perovskite.

Acknowledgements

This work was supported by 973 Program (2014CB643506), the Natural Science Foundation of China (No. 21221063), Program for Chang Jiang Scholars and Innovative Research Team in University (No. IRT101713018), the Graduate Innovation Fund of Jilin University (450060503118) and the Open Project of State Key Laboratory of Supramolecular Structure and Materials (No. sklssm2015019). X.-F. W. and T. M. thank for the support from Japan Science and Technology Agency (JST) Advanced Low Carbon Technology R&D program (ALCA).

Notes and references

[a] State Key Laboratory of Supramolecular Structure and Materials, Jilin University, Changchun 130012, PR China
wjtian@jlu.edu.cn (W. Tian)
[b] Key Laboratory of Physics and Technology for Advanced Batteries, Ministry of Education, College of Physics, Jilin University, Changchun 130012, PR China
xf_wang@jlu.edu.cn(X.-F. Wang)
[c] Graduate School of Engineering, Toin University of Yokohama, 1614 Kurogane-cho, Aoba, Yokohama, Kanagawa 225-8503, Japan

† Electronic Supplementary Information (ESI) available: Supplementary data are provided in the electronic supporting information. See DOI: 10.1039/b000000x/

1 A.Kojima, K.Teshima, Y. Shirai, T.Miyasaka, *J. Am. Chem. Soc*.2009, **131**, 6050−6051.
2 H. S. Kim, C. R. Lee, J. H. Im, K. B. Lee, T. Moehl, A. Marchioro, S. J. Moon, R. Humphry-Baker, J. H. Yum, J. E. Moser, M. Grätzel, N. G. Park, *Sci. Rep.* 2012, **2**, 591.
3 M. M. Lee, J. Teuscher, T. Miyasaka, T. N. Murakami, H. J. Snaith, *Science* 2012, **338**, 643−647.
4 J. H. Heo, S. H. Im, J. H. Noh, T. N. Mandal, C. S. Lim, J. A. Chang, Y. H. Lee, H. Kim, A. Sarkar, M. K. Nazeeruddin, M. Grätzel, S. Seok, *Nat. Photonics* 2013, **7**, 486−491.

5 J. Burschka, N. Pellet, S. J. Moon, R. Humphry-Baker, P. Gao, M. K. Nazeeruddin, M. Grätzel, *Nature* 2013, **499**, 316−319.
6 M. Liu, M. B. Johnston, H. J. Snaith, *Nature* 2013, **501**, 395−398.
7 H. J. Snaith, *J. Phys. Chem. Lett.* 2013, **4**, 3623−3630.
8 P. P. Boix, K. Nonomura, N. Mathews, S. G. Mhaisalkar, *Mater. Today* 2014, **17**, 16−23.
9 S. Kazim, M. K. Nazeeruddin, M. Grätzel, S. Ahmad, *Angew. Chem. Int. Ed.* 2014, **53**, 2812−2824.
10 N.-G. Park, J. Phys. *Chem. Lett.* 2013, **4**, 2423−2429.
11 H.-S. Kim, S. H. Im, N.-G. Park, *J. Phys. Chem. C* 2014, **118**, 5615−5625.
12 H.-S. Kim, C.-R. Lee, J.-H. Im, K.-B. Lee, T. Moehl, A. Marchioro, S.-J. Moon, R. Humphry-Baker, J.-H. Yum, J. E. Moser, M. Grätzel and N.-G. Park, *Sci. Rep.* 2012, **2**, 591/1-591/7.
13 J. M. Ball, M. M. Lee, A. Hey and H. J. Snaith, *Energy Environ. Sci.* 2013, **6**, 1739–1743.
14 W. Zhang , M. Saliba, S. D. Stranks , Y. Sun , X. Shi, U. Wiesner , and H. J. Snaith . *NanoLett.* 2013, **13**, 4505–4510.
15 J.-Y. Jeng, Y. F. Chiang, M. H. Lee, S. R. Peng, T. F. Guo, P. Chen, T. C. Wen, *Adv. Mater.* 2013, **25**, 3727−3732.
16 B. Conings, L. Baeten, C. D. Dobbelaere, J. D'Haen, J. Manca, and H.-G. Boyen, *Adv. Mater.* 2014, **26**, 2041–2046
17 J. Shi, Y. Luo, H. Wei, J. Luo, J. Dong, S. Lv, J. Xiao, Y. Xu, L. Zhu, X. Xu, H. Wu, D. Li, Q. Meng, *ACS Appl. Mater. Interfaces* 2014, **6**, 9711-9718.
18 Z. Xiao, C. Bi, Y. Shao, Q. Dong, Q. Wang, Y. Yuan, C. Wang, Y. Gao, J. Huang, *Energy Environ. Sci.* 2014, **7**, 2619-2623.
19 H. Zhou, Q. Chen, G. Li, S. Luo, T.-b. Song, H.-S. Duan, Z. Hong, J. You, Y. Liu, Y. Yang, *Science* 2014, **345**, 542-546.
20 Q. Hu, J.Wu, C. Jiang, T. Liu, X. Que, R. Zhu, and Q. Gong, *ACS Nano* 2014, **8**, 10161–10167.
21 Q. Chen, H. Zhou, Z. Hong, S. Luo, H.-S. Duan, H.-H. Wang, Y. Liu, G. Li, and Y. Yang, *J. Am. Chem. Soc.* 2014, **136**, 622-625.
22 G. E. Eperon, V. M. Burlakov, P. Docampo, A. Goriely, H. J. Snaith, *Adv. Funct. Mater.* 2014, **24**, 151-157.
23 J. T. W. Wang, J. M. Ball, E. M. Barea, A. Abate, J. A. Alexander-Webber, J. Huang, M. Saliba, I. Mora-Sero, J. Bisquert, H. J. Snaith, R. J. Nicholas, *NanoLett.* 2014,**14**, 724–730.
24 A. Yella, L.-P. Heiniger, P. Gao, M. K. Nazeeruddin, and M. Grätzel, *NanoLett.* 2014, **14**, 2591-2596.
25 D. Y. Liu, T. L. Kelly, *Nat. Photonics.* 2014, **8**, 133–138.
26 D. Y. Liu, M. K. Gangishetty, & T. L. Kelly, *J. Mater. Chem. A* 2014, **2**, 19873-19881.
27 D. Y. Son, J. H. Im, H. S. Kim, N. G. Park, *J. Phys. Chem. C* 2014, **118**,16567–16573.
28 J. Song, J. Bian, E. Zheng, X.-F. Wang, W. Tian, and T. Miyasaka, *Chem. Lett.* 2015, **44**, DOI: 10.1246/cl.150056.
29 C. Kilic, A. Zunger, *Phys. Rev. Lett.* 2002, **88**, 095501.
30 Z. Jarzebski, P. Marton, *J. Electrochem. Soc.* 1976, **123**, 299C.
31 H. L. Hartnagel, A. L. Dewar, A.K. Jain, and C. Jagadish, *Semiconducting Transparent Thin Films* (IOP Publishing, Bristol, 1995).
32 H. J. Snaith, and C. Ducati, *NanoLett.* 2010, **10**, 1259–1265.
33 X.-F. Wang, L. Wang, N. Tamai, O. Kitao, H. Tamiaki, and S. Sasaki, *J. Phys. Chem. C* 2011, **115**, 24394-24402.
34 D. H. Cao, C. C. Stoumpos, C. D. Malliakas, M. J. Katz, O. K. Farha, J. T. Hupp, and M. G. Kanatzidis, *APL Mater.* 2014, **2**, 091101.
35 T. Supasai, N. Rujisamphan, K. Ullrich, A. Chemseddine, and Th. Dittrich, *Appl. Phys. Lett.* 2013, **103**, 183906.
36 Q. Chen, H. Zhou, T.-B. Song, S. Luo, Z. Hong, H.-S. Duan, L. Dou, Y. Liu, Y. Yang, *NanoLett.* 2014, **14**, 4158−4163.
37 L. Wang, C. McCleese, A. Kovalsky, Y. Zhao, and C. Burda, *J. Am. Chem. Soc.* 2014, **136**, 12205−12208.
38 F. Gu, S. F. Wang, C. F. Song, M. K. Lu, Y. X. Qi, G. J. Zhou, D. Xu, D. R. Yuan, *Chem. Phys. Lett.* 2003, **372**, 451–454.
39 G. Li, V. Shrotriya, J. Huang, Y. Yao, T. Moriarty, K. Emery & Y. Yang, *Nature Materials* 2005, **4**, 864-868.
40 C.-H. Chiang, Z.-L. Tseng and C.-G. Wu, *J. Mater. Chem. A* 2014, **2**, 15897–15903.
41 Y. Wu, A. Islam, X. Yang, C. Qin, J. Liu, K. Zhang, W. Peng, L. Han, *Energy Environ. Sci.* 2014, **7**, 2934-2938.
42 Y. Zhao, K. Zhu, *J. Mater. Chem. A* DOI: 10.1039/c4ta05384b.
43 D. Y. Liu, J. L. Yang, and T. L. Kelly, *J. Am. Chem. Soc.* 2014, **136**, 17116−17122.
44 T. Leijtens, G. E. Eperon, S. Pathak, A. Abate, M. M. Lee, H. J. Snaith, *Nature Commun.* 2013, **4**, 2885.
45 S. Chavhan, O.Miguel, H.-J. Grande, V. Gonzalez-Pedro, R. S. S´anchez, E. M. Barea, I. Mora-Ser´o and R. Tena-Zaera, *J. Mater. Chem. A* 2014, **2**, 12754–12760.
46 P. Qin, S. Tanaka, S. Ito, N. Tetreault, K. Manabe, H. Nishino, M. K. Nazeeruddin, M. Grätzel, *Nature Commun.* 2014, **5**, 3834.
47 J. A. Christians, R. C. M. Fung, P. V. Kamat, *J. Am. Chem. Soc.* 2014, **136**, 758-764.